# Landfast ice and coastal wave exposure in northern Alaska

Lucia Hosekova[1], Emily Eidam[2], Gleb panteleev[3], Luc Rainville[4], Rogers Erick[5], and Jim Thomson[4]

[1]Applied Physics Laboratory
[2]University of North Carolina at Chapel Hill
[3]United States Naval Research Laboratory
[4]University of Washington
[5]NRL Stennis

November 21, 2022

**Abstract**

Observations of ocean surface waves at three sites along the northern coast of Alaska show a strong coupling with seasonal sea ice patterns. In the winter, ice cover is complete, and waves are absent. In the spring and early summer, sea ice retreats regionally, but landfast ice persists near the coast. The landfast ice completely attenuates waves formed farther offshore in the open water, causing up to two-month delay in the onset of waves nearshore. In autumn, landfast ice begins to reform, though the wave attenuation is only partial due to lower ice thickness compared to spring. The annual cycle in the observations is reproduced by the ERA5 reanalysis product, but the product does not resolve landfast ice. The resulting ERA5 bias in coastal wave exposure can be corrected by applying a higher resolution ice mask, and this has a significant effect on the long-term trends inferred from ERA5.

# Landfast ice and coastal wave exposure in northern Alaska

**Lucia Hošeková[1], Emily Eidam[2], Gleb Panteleev[3], Luc Rainville[1], W. Erick Rogers[3], Jim Thomson[1]**

[1]Applied Physics Laboratory, University of Washington, Seattle, USA
[2]Department of Marine Sciences, University of North Carolina, Chapel Hill, USA
[3]Naval Research Laboratory, Stennis Space Center, Mississippi, USA

**Key Points:**

- Year-long observations show a seasonal cycle of wave exposure at three sites along the Arctic coast of northern Alaska.
- The persistence of landfast ice in the late spring / early summer dramatically reduces the wave energy reaching the coast.
- Coastal protection by landfast ice is absent from global climate models, however proxy corrections can represent this effect.

Corresponding author: Jim Thomson, `jthomson@apl.washington.edu`

## Abstract

Observations of ocean surface waves at three sites along the northern coast of Alaska show a strong coupling with seasonal sea ice patterns. In the winter, ice cover is complete, and waves are absent. In the spring and early summer, sea ice retreats regionally, but landfast ice persists near the coast. The landfast ice completely attenuates waves formed farther offshore in the open water, causing up to two-month delay in the onset of waves nearshore. In autumn, landfast ice begins to reform, though the wave attenuation is only partial due to lower ice thickness compared to spring. The annual cycle in the observations is reproduced by the ERA5 reanalysis product, but the product does not resolve landfast ice. The resulting ERA5 bias in coastal wave exposure can be corrected by applying a higher resolution ice mask, and this has a significant effect on the long-term trends inferred from ERA5.



## Plain Language Summary

Ocean waves facilitate coastal erosion in the Arctic (and worldwide). Wave energy reaching Arctic coasts is controlled by seasonal sea ice, which includes landfast ice attached to the coastlines or sea floor, and mobile pack ice further seaward. Wave energy in the Arctic is increasing due to loss of pack ice, and these effects are generally well-represented in regional climate models. Landfast ice continues to form at the coast each year, and generally lasts longer than pack ice, providing protection against wave erosion. However, landfast ice is difficult to include in models which can lead them to overestimate the wave energy reaching the coasts. Using observations of waves from three coastal sites in Alaska, we demonstrate the importance of including landfast ice into regional models, and propose an effective method of combining public datasets to account for its effects on waves. These results can help the research community predict how much wave energy will be available for coastal erosion processes in the coming decades.


## 1 Introduction

Arctic coastlines experience rapid rates of erosion, up to tens of meters per year (Jones et al., 2009; Gibbs & Richmond, 2017). The mean retreat rate for coastlines throughout the Arctic is 0.5 m/yr (Lantuit et al., 2012), with highest rates reported in the Laptev (Günther et al., 2013; Nielsen et al., 2020) and Beaufort Seas (Gibbs et al., 2015; Obu et al., 2017). The ice-rich soils are particularly sensitive to thermal niching by seawater at the coastal interface, a process which promotes failure of large blocks of ground along ice wedges (Aré, 1988a, 1988b; Hequette & Barnes, 1990; Günther et al., 2015). Wave energy and storm surges are considered a dominant factor influencing the erosion rate due to their ability to generate and quickly remove sediment (Wobus et al., 2011). In recent decades, summertime pack ice extents in the Arctic have been declining, and the length of the open-water season has been increasing (e.g. (Meier et al., 2013; Barnhart et al., 2016), a trend that is projected to continue. These changes have been linked to an increase in wave climate (Francis et al., 2011; Thomson & Rogers, 2014; Wang et al., 2015; Stopa et al., 2016; Thomson et al., 2016a), and together these effects are expected to drive increasing rates of coastal erosion (Overeem et al., 2011; Barnhart et al., 2014).

Landfast ice buffers the coast against wave energy, particularly during the spring and summer, when open water may be present offshore (Forbes & Taylor, 1994). Landfast ice forms during the fall and generally remains attached to shore (and/or grounded to the seafloor in shallow water) during the winter, though changes in water level and other disturbances may cause it to shift (A. Mahoney et al., 2007). Recent observations suggest that landfast ice is becoming less stable and persists for briefer periods of time both at the beginning and end of of the open-water season (Galley et al., 2012; A. R. Mahoney et al., 2014; Yu et al., 2014). Coastal exposure in the Arctic depends both on the distance of pack ice controlling the wind fetch, and on the presence of landfast ice dissipating the incident wave field. Global reanalysis products used to evaluate effects of waves on coastal erosion do not explicitly represent landfast ice, leading to potential biases in assessing the contributions of waves and their trends.

Here we present observations of wave conditions at three locations along the Alaskan coast throughout the annual cycle and use them to quantify the effects of landfast ice on coastal wave exposure. Section 2 includes description of the sites, experimental setup and datasets used in our analysis. In Section 3.1, we present observed significant wave heights in the context of local ice conditions. In Section 3.2, we compare the observed wave heights to ERA5 dataset and propose a method to reduce its bias in landfast ice covered areas. In Section 4, we apply this approach to correct the estimated decadal trends in wave exposure in ERA5 at one of the sites, and discuss the processes driving seasonal break-up of landfast ice.

## 2 Methods

### 2.1 In-situ dataset

This study focuses on three nearshore sites representative of Arctic sandy barrier island systems (Figure 1(a)). Their locations are in the proximity of the Icy Cape (Chukchi Sea), Jones Islands, and Flaxman Island (Beaufort Sea), and will be referred to as S1, S2 and S3 respectively. The mean long-term (>70 years) erosion rate of the exposed barrier coastlines in northern Alaska is estimated as -1.6 m/yr ($\pm$ 0.73 m/yr) (Gibbs & Richmond, 2017).

Pairs of moorings were deployed at each site between November 2019 and September 2020, as part of the project Coastal Ocean Dynamics in the Arctic (CODA). Each mooring pair consists of a seafloor pressure and temperature logger (RBR duo) located 3 nm (5.5 km) from the shore, and an acoustic Doppler current profiler (Nortek Signature500) on a seafloor tripod, which samples waves, currents and temperature at a distance of 12 nm (22.2 km) from the shore. The moorings were positioned as a cross-shore array, and their locations are further referred to as 'inshore' and 'offshore'. The inshore sites are 14-18 m water depth, and the offshore sites are 25-30 m water depth. The mooring pairs provide a record of inshore and offshore conditions through a full annual cycle of coastal sea ice: refreezing in the fall, full sea ice cover in winter, spring breakup and open water in the summer months.

Wave energy spectra were estimated from the raw pressure and ADCP mooring data, collected at 1 Hz and processed every 30 minutes. The spectral processing uses 256-second windows and merges every three neighboring frequency bands, for an effective 42 degrees of freedom in the resulting spectral estimates. The spectra from the RBR duo bottom pressure measurements at the inshore moorings are converted to sea-surface elevations using the frequency-dependent depth attenuation given by linear wave theory. The highest frequencies ($f > 0.3$ Hz) are too attenuated to measure with bottom pressure in 14-18 m water depth, and thus this portion of each spectra is extrapolated to 0.5 Hz. Significant waves heights $H_s$ are determined from the integral of the energy spectra, and the extrapolation is always less than a 10% adjustment to the reported significant wave height. At the offshore sites, this attenuation and extrapolation correction is unnecessary, because the Nortek Signature500 uses an acoustic altimeter to directly measure sea surface elevations at 1 Hz. For both instrument types, the minimum observable significant wave height is 0.05 m, based on an empirical determination of the noise-floor in the spectra. Any 30-minute record with a calculated $H_s$ less than 0.05 m is considered to be a record without waves present.

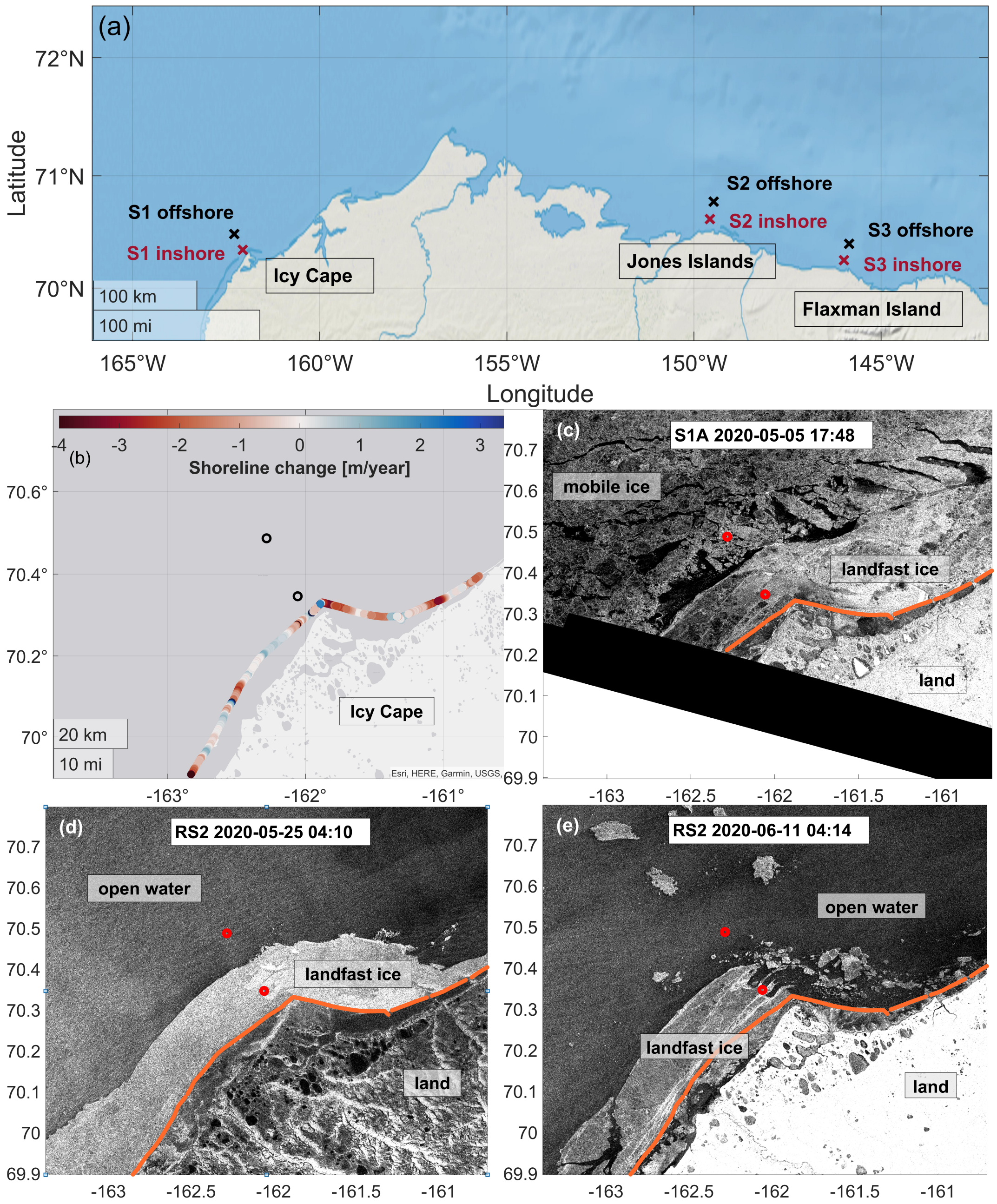


Figure 1: (a) Locations of the mooring sites S1, S2, and S3. (b) Detail of the S1 site, with colors representing rates of exposed shoreline change (Snyder & Gibbs, 2019; Gibbs et al., 2017). (c-e): SAR images acquired by Sentinel-1 and RADARSAT-2 capturing spring breakup of landfast ice in the Icy Cape area. Circles mark locations of S1 moorings. Orange line denotes the exposed shoreline.

Figures 1(b-e) provide detail of the S1 location, the Icy Cape headland in the Chukchi Sea. The regional shoreline is largely erosional (-0.4 m/yr (Gibbs et al., 2015)), with strong variability in exposed shoreline change between the two sides of the headland (Snyder & Gibbs, 2019; Gibbs et al., 2017). The northeast-facing section is characterized by higher erosion rates (up to -4 m/yr), coinciding with its exposure to prevailing wind and wave directions. Figures 1(c-d) show Synthetic-aperture radar (SAR) images provided by Sentinel-1 and RADARSAT-2 detailing three stages of spring sea ice retreat at Icy Cape: 1. formation of the flaw lead 1(c) 2. exposed landfast ice 1(d) 3. break-up of landfast ice 1(e).

The 1 Hz acoustic altimeter data from Nortek Signature500s at the offshore moorings measures ice draft in addition to wave elevations. This contextual data is not used directly in the present analysis, though it is consistent with the SAR images. In particular, the 30-minute mean ice drafts increase throughout the winter to several meters in the months prior to breakup. It is thus likely that the ice closer to shore is at least this thick in the late spring.

### 2.2 Ice and wave products

In Section 3.2, we compare the mooring wave observations to estimates from the atmospheric and wave reanalysis dataset ERA5 (Hersbach et al., 2020) at S1. ERA5 is produced by the European Centre for Medium-Range Weather Forecasts (ECMWF) and provides hourly estimates of atmospheric data, including sea ice concentration, at 0.25 degree grid cell resolution (~30 km), and wave data at 0.5 degrees, and covers the period 1979-present. The ERA5 wave model WAM simulates wind generated wave spectra with 24 directions and 30 frequencies when sea ice concentration is <30% and does not parametrize wave-ice interactions. While at 0.25 degree resolution ERA5 cannot distinguish individual positions of the mooring pairs located 16.6 km apart, it is chosen here as a convenient tool widely used to study multi-decadal evolution of wind, wave and sea ice conditions in the Arctic (e.g. (Kim et al., 2021; Casas-Prat & Wang, 2020)).

In addition to ERA5, we utilize the sea ice concentration product obtained from GOFS 3.1 (Global Ocean Forecasting System, (Metzger et al., 2014)), the U.S. Navy's coupled global ocean-ice forecasting system. Its resolution is 0.08 degrees longitude and 0.04 degrees latitude (~5 km), allowing for a higher accuracy than ERA5 for indicating the presence of coastal sea ice.

SAR satellite imagery provides high resolution (~50 m) representation of the ice conditions every few days. Backscatter characteristics can be used to distinguish open water, sea ice floes, sea ice ridges, leads, and ice type with a high level of detail (e.g., (Kwok et al., 1999)).

Long-term trends in Section 4.1 are estimated by masking ERA5 with sea ice maps provided by the National Snow and Ice Data Center (NSIDC) as a weekly dataset. Sea ice categories are encoded according to the SIGRID-3 format, and include landfast ice boundaries as a vector. The position of the landfast ice is extracted and re-mapped onto the GOFS 3.1 grid and interpolated to daily values.

### 2.3 Coastal wave exposure

Two metrics are used for evaluating the exposure of the coasts to mechanical effects of surface waves. The first is a simple integration of observed and simulated significant wave heights, i.e.

$$\mathcal{H} = \int H_s \Delta t, \tag{1}$$

in units of meter-days, referred to as cumulative wave exposure. It provides an intuitive measure of wave activity, and allows for a straightforward comparison between locations and datasets.

The second metric is the cumulative wave energy, which is calculated from the time integral of wave energy flux incident to the coast,

$$\mathcal{E} = \int E c_g dt, \tag{2}$$

in units of Joules per meter of shoreline. The time series of wave energy density $E$ is determined as

$$E = \frac{\rho g H_s^2}{16}, \tag{3}$$

and the wave group velocity $c_g$ is evaluated using the dispersion relation for intermediate water depth

$$c_g = \frac{L}{2T} + \frac{2\pi d}{T \sinh(4\pi d/L)}, \tag{4}$$

where $\rho$ the density of water, $g$ the gravitational acceleration, $T$ the energy period (first moment) of the reported energy spectrum, $d$ is the water depth at the corresponding mooring location, and $L$ is the wavelength calculated iteratively with inputs of energy period and depth.

# 3 Results

## 3.1 Wave height observations

Significant wave heights at the mooring locations (Figure 1) are shown in Figure 2. In the summer months, significant wave heights are up to 3 m at all sites, consistent with wave climatology for the region (Thomson et al., 2016b). In the winter months, waves are generally not observed, as expected by the verified presence of sea ice at the sites, although there are a few isolated wave events in the winter. The S3 offshore dataset concludes prematurely in August 2020 due to equipment failure.

At S1, both moorings were deployed mid-November 2019 in open water. A series of energetic wave events in November and December coincided with the onset of nearshore pancake sea ice covering the S1 inshore mooring (Hošeková et al., 2020), resulting in partial wave attenuation. The Icy Cape region was fully ice-covered from mid-December until the beginning of May and only sporadic wave activity was detected during this period. In the following two months, the offshore mooring recorded continuous wave activity with significant wave heights of up to 2 m, in contrast to no detectable waves at the inshore mooring location. Satellite imagery obtained by RadarSat 2 and Sentinel 1 show a continuous presence of landfast ice during this period (Figure 1(d-e)), implying complete attenuation of wave energy between the two mooring sites. At the beginning of July, the landfast ice covering the inshore mooring rapidly breaks up and the subsequent wave measurements at the two locations are in agreement for the remainder of the open water season.

At S2, the moorings were deployed during autumn 2019 ice formation, and remained mostly covered by ice until the beginning of July 2020. As at S1, the inshore location was collocated with landfast ice, while the offshore site was covered by mobile ice. On occasion, a flaw lead formed between landfast ice and pack ice and led to sporadic waves detected offshore (only). At the beginning of July, the pack ice retreated and the landfast ice broke off in close succession, resulting in a rapid transition to open water over the period of a week. Waves up to 1 m were detected during this time, and were partially attenuated at the inshore location.

At S3, the flaw lead between landfast ice and pack ice formed a month earlier than at S2 (140 km to the west), allowing for waves to reach the offshore mooring location in early July. As at the other sites, the presence of landfast ice over the inshore mooring led to com-

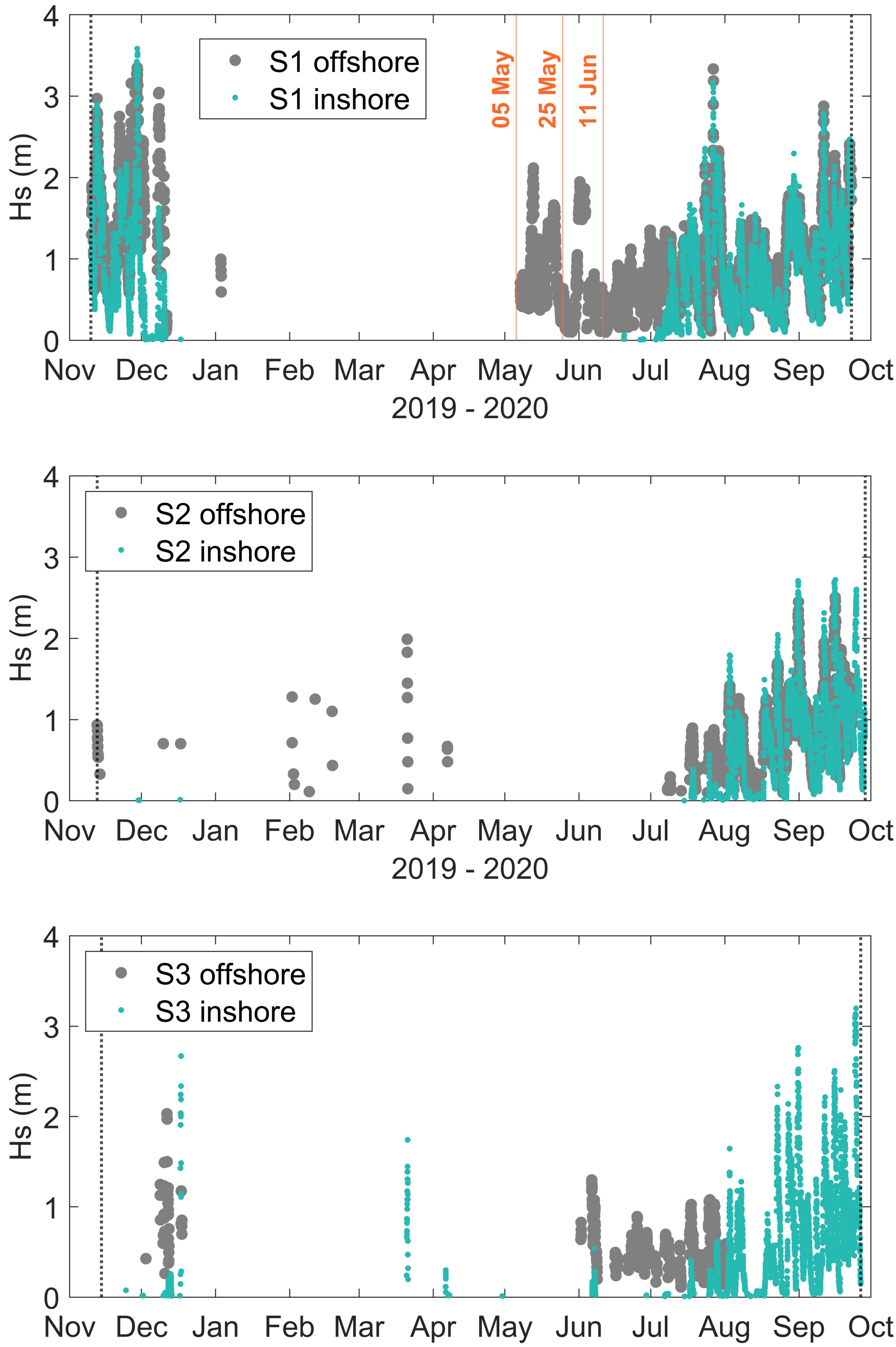


Figure 2: Significant wave heights observed by inshore and offshore moorings at S1, S2 and S3. Orange vertical lines mark dates of SAR imagery from Figure 1. Dotted black lines mark dates of mooring deployments and recoveries.

plete attenuation of the incident wave field. SAR imagery reveals deterioration of the landfast ice at the S3 location through a series of break-up events (see Supporting Information), leaving both mooring locations ice-free by the beginning of July.

The above inference of "complete attenuation" refers to the situation where the wave energy level has become so small that it can no longer be measured using our instrumentation ($H_s < 0.05$ m) and effectively there are no waves at the inshore mooring. In situ observations of attenuation in landfast ice are not common. One exception is Sutherland and Rabault (2016), who report a 12% energy reduction at $f = 0.15$ Hz over a distance of 60 m. Although the ice in our study is much thicker, we can use the Sutherland and Rabault (2016) attenuation rate to assess the theoretical attenuation between the offshore and onshore moorings. The resulting prediction is for $H_s = 2$ m to reduce to the detection threshold of $H_s = 0.05$ m over a distance of 3.4 km. Given the SAR imagery (Figure 1) showing roughly 8 km of landfast ice at Icy Cape, the inference of "complete attenuation" is indeed reasonable.

The CODA dataset demonstrates that coastal waves during the spring transition are limited by both the distance of the offshore ice edge controlling the available wind fetch, and by the presence of landfast ice which prevents the waves from reaching the coast. The contrast between these two factors is particularly evident in the Beaufort Sea locations (S2 and S3) where the onset of offshore waves matches the increasing gap between landfast ice and the drifting pack ice, while the onset of inshore waves is determined by local break-up of landfast ice and occurs almost simultaneously at both sites.

### 3.2 Comparison with ERA5 at S1

In this section, we compare the CODA dataset at the Chukchi Sea location S1 with ERA5 reanalysis, and we consider a modification using the GOFS ice products to make the ERA5 results more consistent with the inshore wave observations. The S1 site was chosen for two reasons: CODA measurements here provide a clear signal contrasting the high wave activity offshore to complete wave attenuation nearshore correlating with the presence of landfast ice; and the rapid decrease in duration of landfast ice reported along the Chukchi coast (4 weeks/decade (Yu et al., 2014)) highlights its relevance as an environmental erosion factor in this region. The results from S2 and S3 are qualitatively similar, though less striking in magnitude.

ERA5 data presented in this section are evaluated hourly at the nearest grid point to the S1 site. The observations are linearly interpolated to the same times. The GOFS dataset was downloaded for daily increments at the time the model assimilates new data (12:00 UTC), and interpolated to hourly intervals.

Figure 3 (a) presents the significant wave heights recorded by the two S1 moorings compared to ERA5 output over spring and summer 2020. Overall, the ERA5 dataset is in good agreement with the wave heights measured by the offshore mooring throughout the entire period, with the exception of a small delay in the initial wave onset in spring due to >30% sea ice concentration reported in the model grid cell. More importantly, ERA5 does not reproduce the difference between the onset of wave activity at the inshore and offshore location, and causing a significant overestimate of inshore waves by ERA5 that persists for two months. This is because both mooring sites are effectively located within a single ERA5 grid cell, and no significant sea ice presence is reported by ERA5 during these months.

The black line in Figure 3(a) demonstrates that the lack of fast ice presence in ERA5 can be rectified by applying a higher resolution sea ice product (i.e. GOFS, see Section 2.2) to mask the waves in the nearshore. The mask here is applied when the mean sea ice concentration exceeds 0% within the GOFS grid cells that bound the inshore mooring location. This approach is based on two assumptions: 1. We assume complete attenuation of the waves incident from offshore. 2. We assume that the nearshore ice cover reported by GOFS during spring transition can be considered to be fast ice, even though GOFS dataset does not explicitly distinguish between ice types. The first assumption is supported by observations. The second assumption is supported by SAR imagery of the CODA sites for the duration of the experiment (see Supporting Information).

Figure 3(b) shows the cumulative wave exposure (Eq. 1) for May through mid-August 2020, as reported by the S1 mooring pair, the ERA5 dataset and the ERA5 corrected using GOFS sea ice concentration as outlined above. The wave exposure metric illustrates the role of landfast ice presence in preventing waves from reaching the coastline: by mid-August the cumulative wave exposure at the inshore location amounted to 46% of that measured offshore. The value reported by ERA5 closely tracks the offshore dataset, while ERA5 in combination with GOFS mask provides a wave exposure estimate resembling the inshore measurements (47% of the offshore value by mid-August). Correcting ERA5 using a high reso-

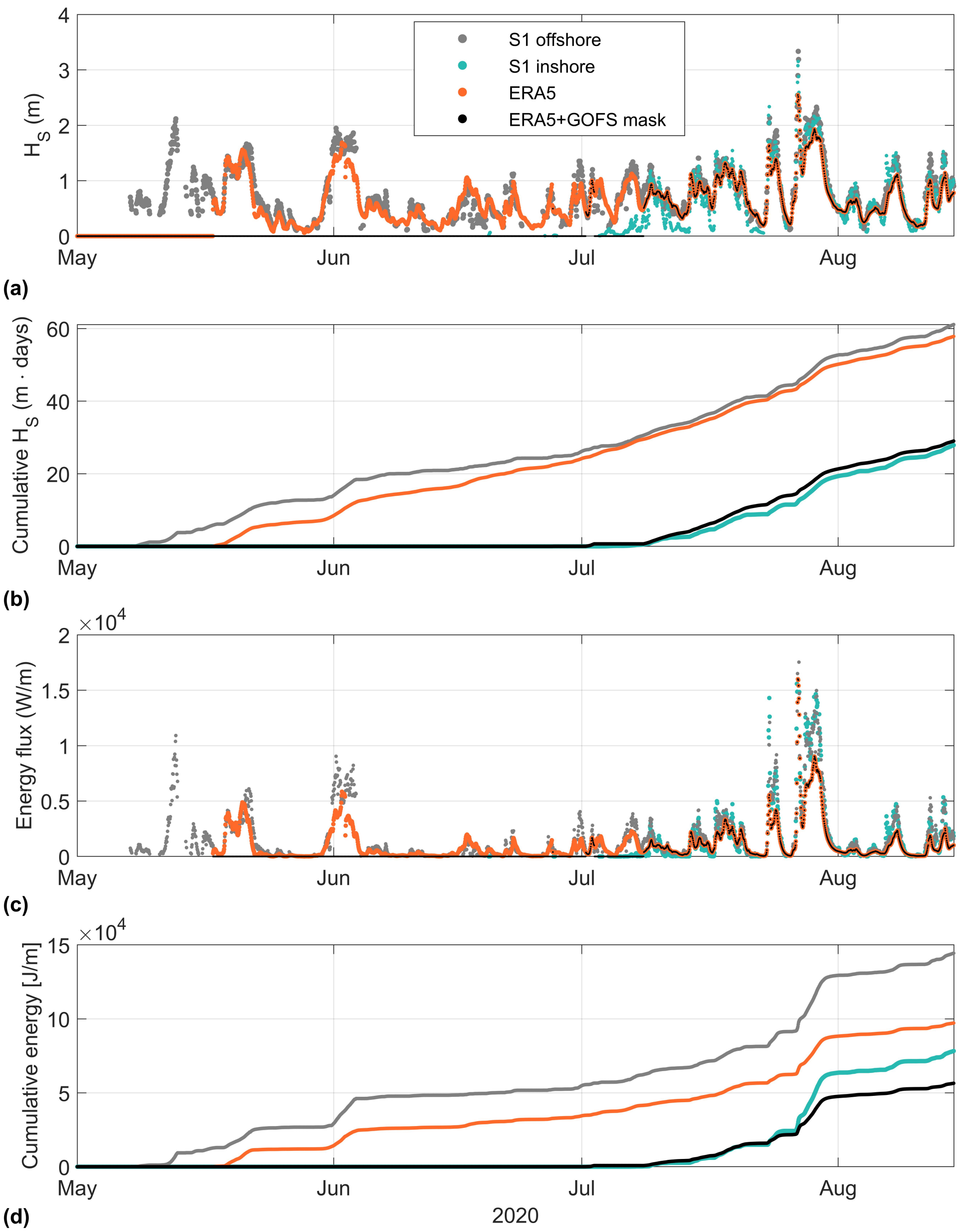


Figure 3: (a) Comparison of observed significant wave heights at S1 and ERA5 reanalysis with and without GOFS sea ice presence mask. All data is interpolated to one hour intervals. (b) Daily commutative sum of wave heights between May 1 - Aug 15 2020. (c) Same as (a) for observed wave energy flux. (d) Same as (c), accumulated daily between May 1 - Aug 15 2020.

lution sea ice product (or ideally, a landfast—ice product) provides more realistic coastal wave exposure than using ERA5 data alone.

Figure 3 further shows the energy flux (c) and cumulative wave energy (d) incident to the Icy Cape headland as reported by instruments at S1 and ERA5 dataset between May - mid-August 2020. The geometry of the headland is taken into account and non-incident wave spectra are discarded (i.e., only the range of $220^\circ < \theta < 100^\circ$ is included). Estimates of wave direction are only available from the offshore mooring, and are used at both mooring locations. Just as shown for the wave exposure metric in Figure 3(b), the presence of landfast ice significantly reduces the cumulative wave energy arriving at the inshore location, by approximately 54% over the spring and summer season.

ERA5 tends to underpredict the offshore energy flux associated with individual wave events (Figure 3(c)), despite its good agreement with offshore $H_s$ measurements (Figure 3(a)). Consequently, only 67% of the total observed offshore energy is reported by ERA5 at the end of the studied time window (Figure 3(d)). While this is closer to the values observed inshore, it is attributed to additional model biases in wave direction and the mean period, rather than an effect of wave attenuation by landfast ice. Accounting for landfast ice presence by applying a GOFS mask, the ERA5 cumulative energy prediction is further reduced to only 39% of the offshore value, considerably lower than the observed 54% inshore.

## 4 Discussion

Here we discuss the implications and limitations of these results for understanding long-term trends and coastal processes. ERA5 is quickly becoming a widely used resource, and there is a related need to ensure that unresolved processes do not cause large biases in results derived from it. The approach is motivated by the strong agreement of ERA5 waves with in situ observations for an entire year at multiple sites, *except* when landfast ice is present.

### 4.1 Long-term trends at S1

The wave observations in Figure 2 suggest that the presence of landfast ice can cause a substantial delay in the spring onset of wave activity along the Alaskan coasts, relative to the seasonal emergence of waves offshore. While the offshore wave energy and number of open water days are increasing in recent decades, it is unclear to what extent this trend is moderated by landfast ice near the coast. Here we explore 41-year long trends in wave presence (as a proxy for open water days), wave exposure and cumulative energy at S1 estimated using ERA5, and apply a correction to account for landfast ice presence based on the masking method outlined in Section 3.2 (Figure 4).

ERA5 datasets for significant wave height, mean wave period based on first moment and mean wave direction are downloaded at 6-hourly intervals, and averaged to obtain daily means for the time period 1979-2020. Because the GOFS sea ice dataset used in Section 3.2 only extends from December 2018 to present and does not explicitly classify landfast ice, we use weekly rasterized landfast ice product from NSIDC (see Section 2.2) instead, covering years 2009-2020.

The long term ERA5 shows evidence of an increasing trend in the number of open water days (5.8 $\pm$ 1.3 days/year), wave exposure (5.1 $\pm$ 1.7 days·m/year) and cumulative wave energy ($1.6{\times}10^4 \pm 1.1{\times}10^4$ J/(m·year)). Despite high inter-annual variability, the trends are qualitatively consistent with other studies showing a comparative increase in open water days and wave heights (Thomson et al., 2016b).

Introduction of the landfast ice mask to ERA5 data at S1 leads to a statistically significant reduction in trend estimates over 2009-2020, despite uncertainties related to inter-annual variability and limited temporal resolution of the landfast ice dataset. The correction is significant to the annual trends, even though the landfast ice mask only corrects a few months per year. The corrected nearshore trends are 1.6 $\pm$ 1.2 days/year for number of open water days, 1.6 $\pm$ 1.3 days·m/year for wave exposure, and $3.5{\times}10^3 \pm 6.5{\times}10^3$ J/(m·year) for cumulative wave energy. This is of particular relevance to studies that rely on reanalysis datasets and model projections to evaluate long-term erosive effects of waves.

### 4.2 Spring break-up of landfast ice

Expanding these methods beyond a simple ice-mask will require more detailed treatment of the landfast ice processes and coupling with other coastal processes. Coastal protection by landfast ice is intrinsically tied to the evolution of the ice itself. When landfast ice is present, the seawater temperatures are maintained at or near the freezing point, and processes such as thermal niching of permafrost bluffs are inhibited. The seasonal breakout of landfast ice can be driven by either mechanical (waves, winds, currents) or thermal (solar radiation, advected/upwelled warm water) forcing. Thus, multiple feedbacks are possible, including the grounding of the landfast ice in shallow water that may enhance persis-

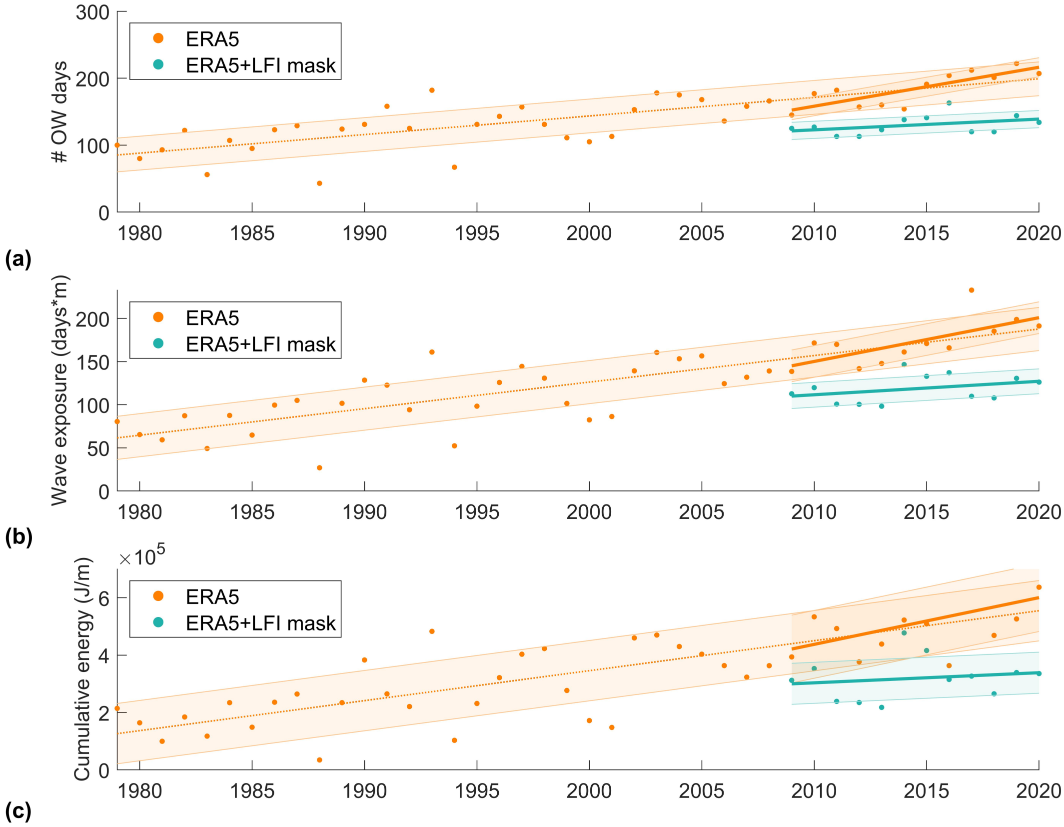


Figure 4: (a) Number of open water days at S1 reported by ERA5 with and without correcting for landfast ice (green and orange, respectively). (b) Same as (a) for coastal wave exposure at S1. (c) Same as (a) for cumulative energy incident to Icy Cape headland. Trend lines are evaluated using linear regression for 1979-2020 (dotted) and 2009-2020 (solid). Shaded areas correspond to standard error of the regression.

tence at specific sites. The CODA dataset includes observations of rapid increases in water temperature coincident with the retreat of the landfast ice (see Supporting Information), though it is not clear if this is a cause or a consequence. The clear signal reported and applied here is simply that landfast ice causes persistent coastal protection from wave action that is not resolved by global climate models.

## 5 Conclusions

Observations of ocean surface waves at multiple sites along Arctic coast of Alaska demonstrate that:

- The seasonal wave climate is controlled by both the distance from pack ice and the attenuation within nearshore ice.
- During spring melt season, we observed complete attenuation of the incident wave field by landfast ice, delaying wave activity at the coast by up to 60 days.
- While ERA5 reanalysis shows good agreement with observed offshore wave heights, it fails to reproduce the delayed wave onset at the coast due to unresolved landfast ice. This results in ERA5 overestimating the cumulative spring coastal wave exposure by up to 47% compared to observations.
- Applying a landfast ice mask derived from a high resolution sea ice product (e.g. GOFS, NIC) to ERA5 significantly reduces the bias in reported wave exposure and number of open water days.
- The lack of landfast ice information causes ERA5 to overestimate the inter-annual trend in the number of open water days by up to 72% at the Chukchi Sea coast.

These results can be applied to improve understanding of coastal change in the emerging Arctic.

## Acknowledgments

LH and JT were funded by US National Science Foundation (OPP 1818485). GP and ER were funded by the Office of Naval Research, Program Elements 62435N and 0601153N. LR was funded by the Office of Naval Research grant N000141612377.

Data are available from `http://hdl.handle.net/1773/47139`.

See Supporting Information for an extended list of acknowledgements.

## References

Aré, F. E. (1988a). Thermal abrasion of sea coasts (part i). *Polar Geography and Geology*, *12*(1), 1-1. Retrieved from https://doi.org/10.1080/10889378809377343 doi: 10.1080/10889378809377343

Aré, F. E. (1988b). Thermal abrasion of sea coasts (part ii). *Polar Geography and Geology*, *12*(2), 87-87. Retrieved from https://doi.org/10.1080/10889378809377352 doi: 10.1080/10889378809377352

Barnhart, K. R., Miller, C. R., Overeem, I., & Kay, J. E. (2016, 3). Mapping the future expansion of Arctic open water. *Nature Climate Change*, *6*, 280-285. Retrieved from www.nature.com/natureclimatechange doi: 10.1038/nclimate2848

Barnhart, K. R., Overeem, I., & Anderson, R. S. (2014). The effect of changing sea ice on the physical vulnerability of Arctic coasts. *The Cryosphere*, *8*(5), 1777–1799. Retrieved from https://www.the-cryosphere.net/8/1777/2014/ doi: 10.5194/tc-8-1777-2014

Casas-Prat, M., & Wang, X. L. (2020). Projections of extreme ocean waves in the Arctic and potential implications for coastal inundation and erosion. *Journal of Geophysical Research: Oceans*, *125*(8), e2019JC015745. Retrieved from https://agupubs.onlinelibrary.wiley.com/doi/abs/10.1029/2019JC015745 (e2019JC015745 10.1029/2019JC015745) doi: https://doi.org/10.1029/2019JC015745

Forbes, D., & Taylor, R. (1994). Ice in the shore zone and the geomorphology of cold coasts. *Progress in Physical Geography: Earth and Environment*, *18*(1), 59-89. Retrieved from https://doi.org/10.1177/030913339401800104 doi: 10.1177/030913339401800104

Francis, O. P., Panteleev, G. G., & Atkinson, D. E. (2011). Ocean wave conditions in the Chukchi Sea from satellite and in situ observations. *Geophys. Res. Lett.*, *38*(L24610). doi: 10.1029/2011GL049839

Galley, R. J., Else, B. G., Howell, S. E., Lukovich, J. V., & Barber, D. G. (2012, 6). Landfast sea ice conditions in the Canadian Arctic: 1983-2009. *Arctic*, *65*, 133-144. Retrieved from http://ec.gc.ca/glaces-ice/ doi: 10.14430/arctic4195

Gibbs, A. E., Ohman, K. A., Coppersmith, R., & Richmond, B. M. (2017). *A GIS compilation of updated vector shorelines and associated shoreline change data for the north coast of Alaska, U.S. Canadian border to Icy Cape.* U.S. Geological Survey data release. doi: 10.5066/F72Z13N1

Gibbs, A. E., Ohman, K. A., & Richmond, B. M. (2015). *National assessment of shoreline change—a GIS compilation of vector shorelines and associated shoreline change data for the north coast of Alaska, U.S.-Canadian border to Icy Cape* (Open-File Report No. 2015-1030). U.S. Geological Survey. doi: http://dx.doi.org/10.3133/ofr20151030

Gibbs, A. E., & Richmond, B. M. (2017). *National assessment of shoreline change -— Summary statistics for updated vector shorelines and associated shoreline change data for the north coast of Alaska, U.S.-Canadian border to Icy Cape: U.s. geological survey open-file report 2017–1107* (Open-File Report No. 2017–1107). U.S. Geological Survey. doi: https://doi.org/10.3133/ofr20171107

Günther, F., Overduin, P. P., Sandakov, A. V., Grosse, G., & Grigoriev, M. N. (2013). Short- and long-term thermo-erosion of ice-rich permafrost coasts in the Laptev sea region. *Biogeosciences*, *10*(6), 4297–4318. Retrieved from `https://bg.copernicus.org/articles/10/4297/2013/` doi: 10.5194/bg-10-4297-2013

Günther, F., Overduin, P. P., Yakshina, I. A., Opel, T., Baranskaya, A. V., & Grigoriev, M. N. (2015). Observing Muostakh disappear: permafrost thaw subsidence and erosion of a ground-ice-rich island in response to Arctic summer warming and sea ice reduction. *The Cryosphere*, *9*(1), 151–178. Retrieved from `https://tc.copernicus.org/articles/9/151/2015/` doi: 10.5194/tc-9-151-2015

Hequette, A., & Barnes, P. W. (1990). Coastal retreat and shoreface profile variations in the Canadian Beaufort sea. *Marine Geology*, *91*(1), 113-132. Retrieved from `https://www.sciencedirect.com/science/article/pii/0025322790901368` doi: https://doi.org/10.1016/0025-3227(90)90136-8

Hersbach, H., Bell, B., Berrisford, P., Hirahara, S., Horányi, A., Muñoz-Sabater, J., … Thépaut, J.-N. (2020). The ERA5 global reanalysis. *Quarterly Journal of the Royal Meteorological Society*, *146*(730), 1999-2049. Retrieved from `https://rmets.onlinelibrary.wiley.com/doi/abs/10.1002/qj.3803` doi: https://doi.org/10.1002/qj.3803

Hošeková, L., Malila, M. P., Rogers, W. E., Roach, L. A., Eidam, E., Rainville, L., … Thomson, J. (2020). Attenuation of ocean surface waves in pancake and frazil sea ice along the coast of the Chukchi Sea. *Journal of Geophysical Research: Oceans*, *125*(12), e2020JC016746. Retrieved from `https://agupubs.onlinelibrary.wiley.com/doi/abs/10.1029/2020JC016746` (e2020JC016746

2020JC016746) doi: https://doi.org/10.1029/2020JC016746

Jones, B. M., Arp, C. D., Jorgenson, M. T., Hinkel, K. M., Schmutz, J. A., & Flint, P. L. (2009). Increase in the rate and uniformity of coastline erosion in Arctic Alaska. *Geophysical Research Letters*, *36*(3). Retrieved from http://dx.doi.org/10.1029/2008GL036205 (L03503) doi: 10.1029/2008GL036205

Kim, J., Murphy, E., Nistor, I., Ferguson, S., & Provan, M. (2021). Numerical analysis of storm surges on canada's western arctic coastline. *Journal of Marine Science and Engineering*, *9*(3). Retrieved from https://www.mdpi.com/2077-1312/9/3/326 doi: 10.3390/jmse9030326

Kwok, R., Cunningham, G. F., LaBelle-Hamer, N., Holt, B., & Rothrock, D. (1999). Ice thickness derived from high-resolution radar imagery. *Eos, Transactions American Geophysical Union*, *80*(42), 495-497. Retrieved from https://agupubs.onlinelibrary.wiley.com/doi/abs/10.1029/EO080i042p00495-01 doi: https://doi.org/10.1029/EO080i042p00495-01

Lantuit, H., Overduin, P. P., Couture, N., Wetterich, S., Aré, F., Atkinson, D., … Vasiliev, A. (2012). The Arctic coastal dynamics database: A new classification scheme and statistics on Arctic permafrost coastlines. *Estuaries and Coasts*, *35*(2), 383–400. Retrieved from http://www.jstor.org/stable/41486638

Mahoney, A., Eicken, H., & Shapiro, L. (2007). How fast is landfast sea ice? A study of the attachment and detachment of nearshore ice at Barrow, Alaska. *Cold Regions Science and Technology*, *47*(3), 233-255. Retrieved from https://www.sciencedirect.com/science/article/pii/S0165232X06001431 doi: https://doi.org/10.1016/j.coldregions.2006.09.005

Mahoney, A. R., Eicken, H., Gaylord, A. G., & Gens, R. (2014). Landfast sea ice extent in the Chukchi and Beaufort Seas: The annual cycle and decadal variability. *Cold Regions Science and Technology*, *103*, 41-56. Retrieved from https://www.sciencedirect.com/science/article/pii/S0165232X14000585 doi: https://doi.org/10.1016/j.coldregions.2014.03.003

Meier, W., Gallaher, D., & Campbell, G. G. (2013). New estimates of Arctic and Antarctic sea ice extent during september 1964 from recovered Nimbus I satellite imagery. *The Cryosphere*, *7*, 699-705. doi: 10.5194/tc-7-699-2013

Metzger, E. J., Smedstad, O. M., Thoppil, P. G., Hurlburt, H. E., Cummings, J. A., Wallcraft, A. J., … DeHaan, C. J. (2014, September). US Navy operational global ocean and Arctic ice prediction systems. *Oceanography*. Retrieved from https://doi.org/10.5670/oceanog.2014.66

Nielsen, D. M., Dobrynin, M., Baehr, J., Razumov, S., & Grigoriev, M. (2020). Coastal erosion variability at the southern Laptev Sea linked to winter sea ice and the Arctic oscillation. *Geophysical Research Letters*, *47*(5), e2019GL086876. Retrieved from https://agupubs.onlinelibrary.wiley.com/doi/abs/10.1029/2019GL086876 (e2019GL086876 10.1029/2019GL086876) doi: https://doi.org/10.1029/2019GL086876

Obu, J., Lantuit, H., Grosse, G., Günther, F., Sachs, T., Helm, V., & Fritz, M. (2017). Coastal erosion and mass wasting along the Canadian Beaufort Sea based on annual airborne LiDAR elevation data. *Geomorphology*, *293*, 331-346. Retrieved from https://www.sciencedirect.com/science/article/pii/S0169555X16300502 (Permafrost and periglacial research from coasts to mountains) doi: https://doi.org/10.1016/j.geomorph.2016.02.014

Overeem, I., Anderson, R. S., Wobus, C. W., Clow, G. D., Urban, F. E., & Matell, N. (2011). Sea ice loss enhances wave action at the Arctic coast. *Geophysical Research Letters*, *38*(17). Retrieved from http://dx.doi.org/10.1029/2011GL048681 doi: 10.1029/2011GL048681

Snyder, A. G., & Gibbs, A. E. (2019). *National assessment of shoreline change: A GIS compilation of updated vector shorelines and associated shoreline change data for the north coast of Alaska, Icy Cape to Cape Prince of Wales.* U.S. Geological Survey data release. doi: 10.5066/P9H1S1PV

Stopa, J. E., Ardhuin, F., & Girard-Adrhuin, F. (2016). Wave-climate in the Arctic 1992-2014: seasonality, trends, and wave-ice influence. *The Cryosphere*, *10*(4), 1605-1629. doi: 10.5194/tc-10-1605-2016

Sutherland, G., & Rabault, J. (2016). Observations of wave dispersion and attenuation in landfast ice. *Journal of Geophysical Research: Oceans*. Retrieved from http://dx.doi.org/10.1002/2015JC011446 doi: 10.1002/2015JC011446

Thomson, J., Fan, Y., Stammerjohn, S., Stopa, J., Rogers, W. E., Girard-Ardhuin, F., … Bidlot, J.-R. (2016a). Emerging trends in the sea state of the Beaufort and Chukchi seas. *Ocean Modelling*, *105*, 1 - 12. Retrieved from http://www.sciencedirect.com/science/article/pii/S1463500316300622 doi: https://doi.org/10.1016/j.ocemod.2016.02.009

Thomson, J., Fan, Y., Stammerjohn, S., Stopa, J., Rogers, W. E., Girard-Ardhuin, F., … Bidlot, J.-R. (2016b). Emerging trends in the sea state of the Beaufort and Chukchi seas. *Ocean Modelling*, *105*, 1 - 12. Retrieved from `http://www.sciencedirect.com/science/article/pii/S1463500316300622` doi: http://dx.doi.org/10.1016/j.ocemod.2016.02.009

Thomson, J., & Rogers, W. E. (2014). Swell and sea in the emerging Arctic Ocean. *Geophysical Research Letters*. Retrieved from `http://dx.doi.org/10.1002/2014GL059983` doi: 10.1002/2014GL059983

Wang, X. L., Feng, Y., Swail, V. R., & Cox, A. (2015, 08). Historical changes in the Beaufort-Chukchi-Bering seas surface winds and waves, 1971-2013. *Journal of Climate*. Retrieved from `http://dx.doi.org/10.1175/JCLI-D-15-0190.1` doi: 10.1175/JCLI-D-15-0190.1

Wobus, C., Anderson, R., Overeem, I., Matell, N., Clow, G., & Urban, F. (2011). Thermal erosion of a permafrost coastline: Improving process-based models using time-lapse photography. *Arctic, Antarctic, and Alpine Research*, *43*(3), 474-484. Retrieved from `https://doi.org/10.1657/1938-4246-43.3.474` doi: 10.1657/1938-4246-43.3.474

Yu, Y., Stern, H., Fowler, C., Fetterer, F., & Maslanik, J. (2014). Interannual variability of Arctic landfast ice between 1976 and 2007. *Journal of Climate*, *27*(1), 227 - 243. Retrieved from `https://journals.ametsoc.org/view/journals/clim/27/1/jcli-d-13-00178.1.xml` doi: 10.1175/JCLI-D-13-00178.1

# Supporting Information for ”Landfast ice and coastal wave exposure in northern Alaska”

Lucia Hošeková[1], Emily Eidam[2], Gleb Panteleev[3], Luc Rainville[1], W. Erick Rogers[3], Jim Thomson[1]

[1]Applied Physics Laboratory, University of Washington, Seattle, USA

[2]Department of Marine Sciences, University of North Carolina, Chapel Hill, USA

[3]Naval Research Laboratory, Stennis Space Center, Mississippi, USA

## Contents of this file

1. Figures SF1 and SF2
2. Tables ST1 and ST2
3. Text SA1

## Additional Supporting Information (Files uploaded separately)

1. Captions for Movies SM1 to SM3

**Introduction** This supporting information includes additional observations collected at sites S1-3 and datasets corroborating our analysis.

Figure SF1 shows long term trends in three wave exposure metrics calculated using ERA5 reanalysis at the S1 location, with and without a correction for landfast ice presence (denoted as 'LFI mask'). The three metrics are (a) number of open water days, (b) cumulative wave exposure, and (c) cumulative energy. The figure shows a comparison between annual values and their respective trends, and those aggregated only over January-August (corresponding to spring/summer). Estimated trends obtained using linear regression between 2009-2020 are shown in Table ST2.

Figure SF2 presents temperatures recorded near seafloor using temperature loggers (Onset HOBOs) at the inshore and offshore S1 moorings during sea ice melt, and compares them to sea surface temperatures reported by ERA5 at S1.

Table ST1 contains geographical coordinates and depths of the six moorings, deployed in pairs 3 nm (5.5 km; inshore) and 12 nm (22.2 km; offshore) from the coast at S1-3.

Table ST2 lists the inter-annual trends of the wave exposure metrics in Figure SF1. The estimated trends are obtained using linear regression and include only years 2009-2020 as per availability of the landfast ice data.

**Text SA1.** Extended acknowledgements

We thank the captain and crew of *R/V Sikuliaq*, as well as the ship's marine technicians and engineer Alex de Klerk for their support. We thank our colleague Nirni Kumar for his contributions and friendship. We kindly thank John and Becca Guillote from Onpoint Outreach for documenting our work on `www.iceinmotion.com`.

ERA5 results generated using Copernicus Climate Change Service information 2020, publicly available at `https://cds.climate.copernicus.eu/`. Funding for the development of HYCOM has been provided by the National Ocean Partnership Program and the Office of Naval Research. Data assimilative products using HYCOM are funded by the U.S. Navy. Computer time was made available by the DoD High Performance Computing Modernization Program. The output is publicly available at `https://hycom.org`. Weekly sea ice maps produced by NSIDC are available from World Data Center at Arctic and Antarctic Research Institute `http://wdc.aari.ru/datasets/d0032/arctic/`. Satellite ice images and analysis were provided via special support from the U.S National Ice Center. RADARSAT-2 Data and Products are under a copyright of MDA Geospatial Services Inc. 2019-2020 – All Rights Reserved, obtained via the U.S. National Ice Center. RADARSAT is an official mark of the Canadian Space Agency. Sentinel-1 data was obtained from the Copernicus Data Hub, supported by the European Space Agency.

Environmental sensor data from the Coastal Ocean Dynamics in the Arctic (CODA) 2020 cruise is available from the Rolling Deck to Repository (R2R) archive `https://www.rvdata.us/search/cruise/SKQ202013S`.

**Movie SM1.** Top: SAR imagery at site S1 during sea ice melt season. Bottom: Significant wave heights observed at S1 at the offshore and inshore mooring location.

**Movie SM2.** Top: SAR imagery at site S2 during sea ice melt season. Bottom: Significant wave heights observed at S2 at the offshore and inshore mooring location.

**Movie SM3.** Top: SAR imagery at site S3 during sea ice melt season. Bottom: Significant wave heights observed at S3 at the offshore and inshore mooring location.

| Site | Depth | Latitude | Longitude |
|---|---|---|---|
| S1 inshore | 13 m | 70.346097° | -162.057218° |
| S1 offshore | 30 m | 70.486942° | -162.282848° |
| S2 inshore | 14 m | 70.619651° | -149.575476° |
| S2 offshore | 20 m | 70.774131° | -149.477018° |
| S3 inshore | 21 m | 70.252539° | -145.994910° |
| S3 offshore | 34 m | 70.399441° | -145.856796° |

**Table ST1.** Geographical coordinates and depths of the inshore and offshore moorings deployed at sites S1, S2 and S3.

| | OW days (days/year) | Wave exposure (days·m/year) | Energy (J/(m·year)) |
|---|---|---|---|
| ERA5 (Jan-Dec) | 6(1) | 5(2) | $2(1)\times10^4$ |
| ERA5+LFI (Jan-Dec) | 2(1) | 2(1) | $4(7)\times10^3$ |
| ERA5 (Jan-Aug) | 3(1) | 2(1) | $3(3)\times10^3$ |
| ERA5+LFI (Jan-Aug) | 0.1(8) | 0.1(7) | $1(3)\times10^3$ |

**Table ST2.** Inter-annual trends in the number of open water days, coastal wave exposure and cumulative wave energy at S1 between 2009-2020 estimated from ERA5 and ERA5 corrected for the presence of landfast ice (ERA5+LFI). The trends were obtained using linear regression using cumulative values over the entire year or melt season only (Jan-Aug). The standard errors of regression are shown in brackets and affect the last digit of the respective result.

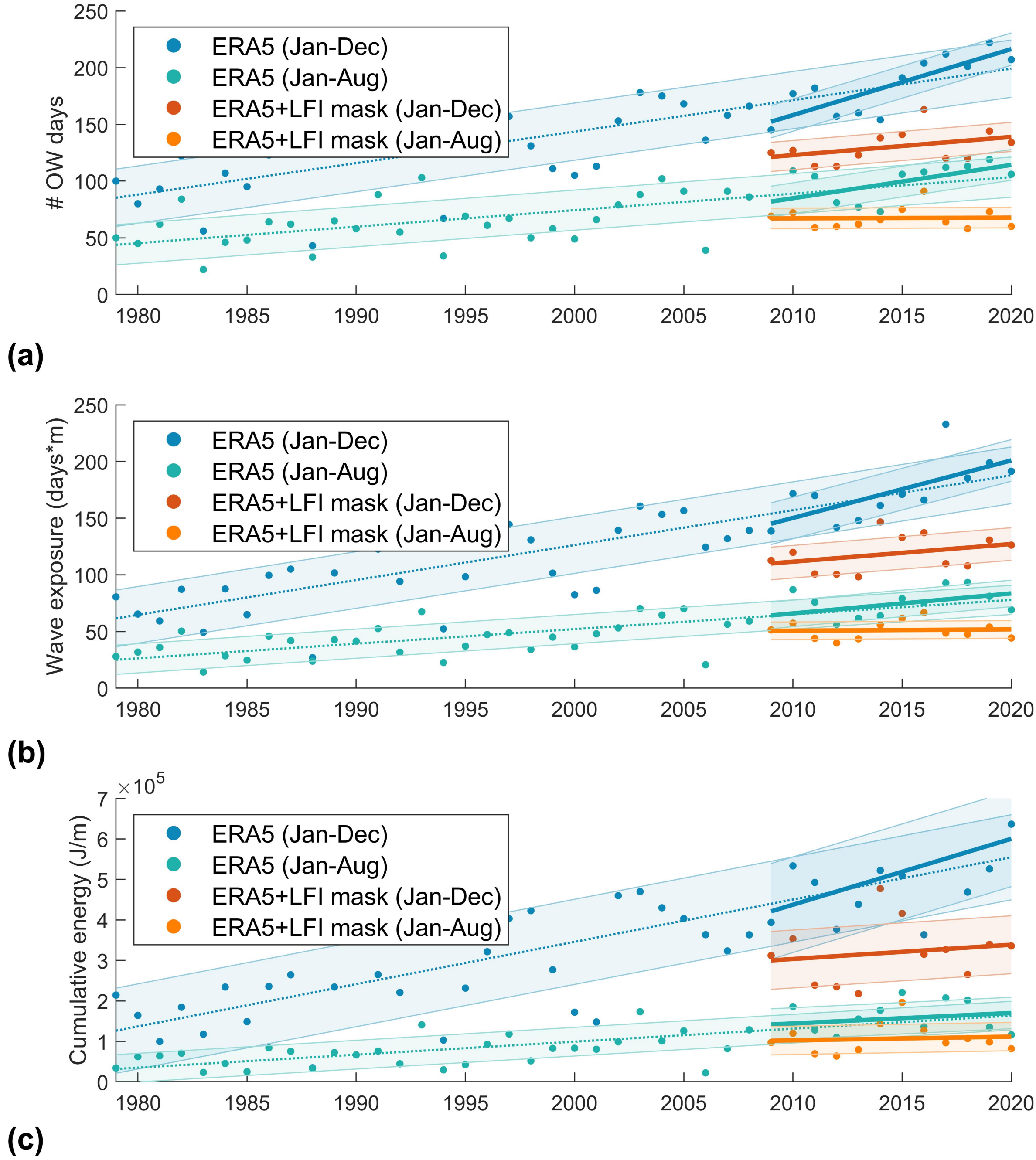


**Figure SF1.** (a) Number of open water days at S1 reported by ERA5 with and without correcting for landfast ice (blue and red, respectively), compared the same for ice melt season only (green and orange, respectively). (b) Same as (a) for coastal wave exposure at S1. (c) Same as (a) for cumulative energy incident to Icy Cape headland. Trend lines evaluated using linear regression for 1979-2020 (dotted) and 2009-2020 (solid). Shaded areas correspond to standard error of the regression.

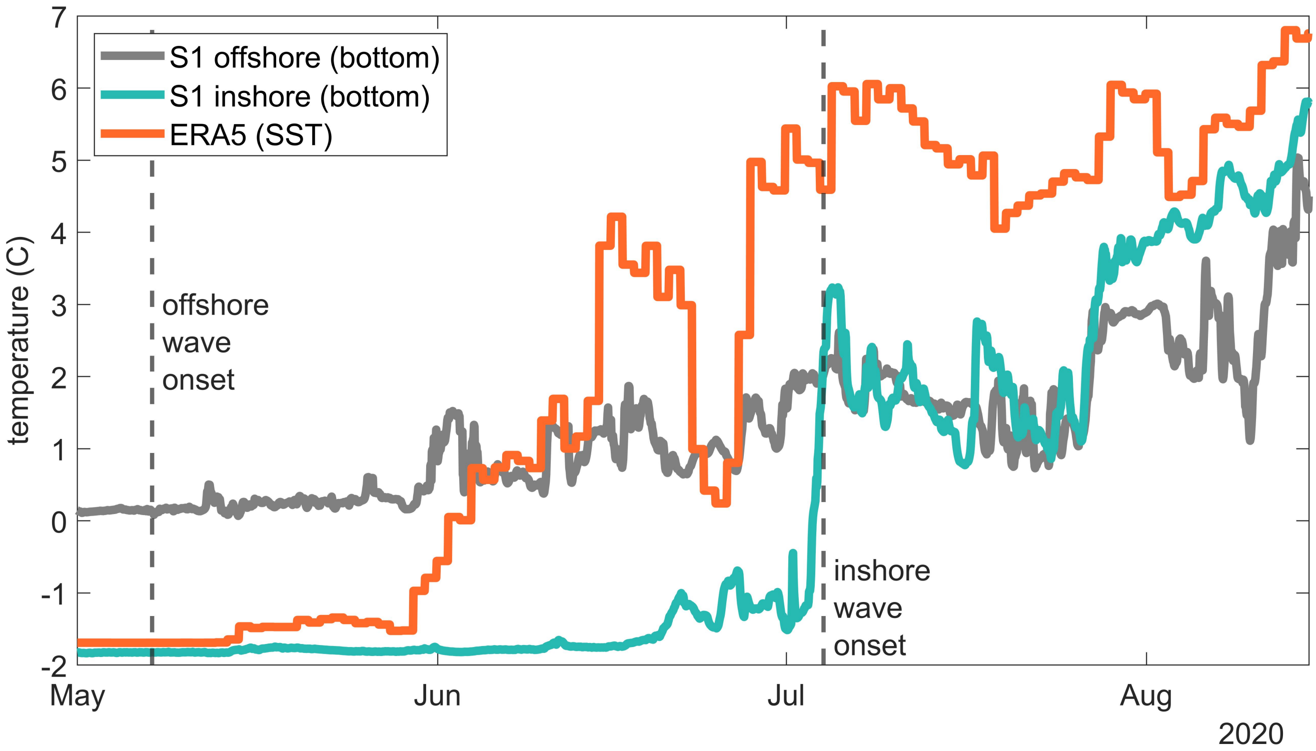


**Figure SF2.** Temperature at S1 during sea ice retreat in 2020 as observed at 30 m depth offshore (orange), at 13 m depth inshore (grey), and as reported by ERA5 at the surface (green). Dotted lines mark the onset of waves with $H_s > 0.1$ m observed by the inshore and offshore moorings.